aerospace

Article

The Influence of External Flow Field on the Flow Separation of Overexpanded Single-Expansion Ramp Nozzle

Yang Yu [1,*], Yuepeng Mao [2], Tao Yu [1], Yalin Yang [1], Shulin Xu [3] and Sijia Liang [3]

[1] School of Aeronautics, Chongqing Jiaotong University, Chongqing 400074, China; yutao@mails.cqjtu.edu.cn (T.Y.); 622210991013@mails.cqjtu.edu.cn (Y.Y.)
[2] Computational Aerodynamics Institute, China Aerodynamics Research and Development Center, Mianyang 621010, China; yuepengmao@126.com
[3] The Green Aerotechnics Research Institute of Chongqing Jiaotong University, Chongqing Key Laboratory of Green Aviation Energy and Power, Chognqing 401120, China; xutreeview@126.com (S.X.); liangsijia17@163.com (S.L.)
* Correspondence: yuyang227@vip.sina.com

Abstract: Flow separation and transitions of separation patterns are common phenomena of nozzles working with a wide Mach range. The maximum thrust method is applied to design the single-expansion ramp nozzle (SERN) for specific operating conditions. The nozzle is used to numerically simulate the transition processes of separation patterns under the linear change in the external flow Mach number and the actual trajectory take-off condition of a rocket-based combined cycle (RBCC), to investigate the mechanism through which the external flow field influences the separation pattern transition during acceleration. The computational fluid dynamics (CFD) method is briefly introduced, followed by experimental validation. Then, the design procedure of SERN is described in detail. The simulation results indicate that as the external Mach number increases, the flow field in the nozzle undergoes transitions from RSS (ramp) to FSS, and finally exhibits a no-flow separation pattern. The rate at which the external Mach number varies has little effect on the transition principle of the nozzle flow separation patterns, but it has a significant effect on the critical Mach number of the transition points. The external flow field of the nozzle has an airflow accumulation effect during acceleration, which can delay the transition of the flow separation pattern.

Keywords: overexpansion state; flow separation; single-expansion ramp nozzle (SERN); external flow; numerical simulation

check for updates

Citation: Yu, Y.; Mao, Y.; Yu, T.; Yang, Y.; Xu, S.; Liang, S. The Influence of External Flow Field on the Flow Separation of Overexpanded Single-Expansion Ramp Nozzle. *Aerospace* **2023**, *10*, 958. https://doi.org/10.3390/aerospace10110958

Academic Editor: Konstantinos Kontis

Received: 24 September 2023
Revised: 6 November 2023
Accepted: 10 November 2023
Published: 13 November 2023

1. Introduction

Speed is an important index to measure the performance of aircraft, so hypersonic flight technology has attracted much attention [1,2]. The scramjet engine is one of the most ideal power sources for hypersonic vehicles because of its simple configuration and excellent efficiency at high Mach numbers. However, the scramjet operates within a narrow range of Mach numbers and needs to reach a high flight Mach number before startup. As a result, hypersonic vehicles powered by scramjet engines are forced to use other types of booster devices, drastically limiting flexibility and increasing operating costs. Therefore, researchers proposed the concept of combined cycle engines [3], which successfully combine several propulsion units and exploit the characteristics of each unit to maintain high thrust and specific impulse throughout the flight process.

The RBCC engine combines the advantages of rocket engine with high thrust-to-weight ratio and ramjet with high specific impulse to operate over a wide Mach range. Considering the requirement for the integrated installation of the aircraft and the nozzle, the afterbody of the aircraft is typically designed as the expansion ramp of SERN. This not only helps reduce the weight of the aircraft but also provides a certain self-stabilization for the engine during off-design operations [4]. With the support of numerous experiments, the GTX scheme [5] and the ISTAR scheme [6] for RBCC were determined to achieve the thermal throat via combustion and to reach the required thrust and specific impulse using the SERN with a fixed geometric structure. The SERN is the main thrust component of the hypersonic propulsion system, so the design of the nozzle is very important [7]. The design point of the nozzle is slightly smaller than the cruise Mach number [8], which makes the SERN work in a serious overexpansion state at low flight Mach number. Due to the reverse pressure gradient, flow separation is bound to occur. The shock wave/boundary layer interaction (SWBLI) will cause unsteady flow in the nozzle [9,10]. The separation caused by the shock wave will also produce unsteady force, reducing the service life of the nozzle [11].

Concerning overexpansion flow separation, early research focused mostly on the axisymmetric rocket nozzle. Studies have suggested that there are two distinct patterns of separation, namely free shock separation (FSS) and restricted shock separation (RSS) [12,13], with FSS being the more common pattern. In addition to the traditional axisymmetric rocket nozzle, symmetric and asymmetric flow separation structures were also observed in two-dimensional convergence–diffusion channel experiments [14]. Similarly, FSS and RSS also exist in SERN, with RSS (ramp) being the most common. FSS requires an extremely narrow range of nozzle pressure ratios (NPR), so some nozzles do not appear. Restricted shock separation with the separation bubble forming on the flap (RSS (flap)) will be present in SERN with a lengthy flap. In a previous study [15], the authors observed the transition from RSS (ramp) to RSS (flap) during the nozzle shutdown process, as illustrated in Figure 1. The transition was instantaneous, which resulted in a mutation in nozzle performance and hindered stable flight.

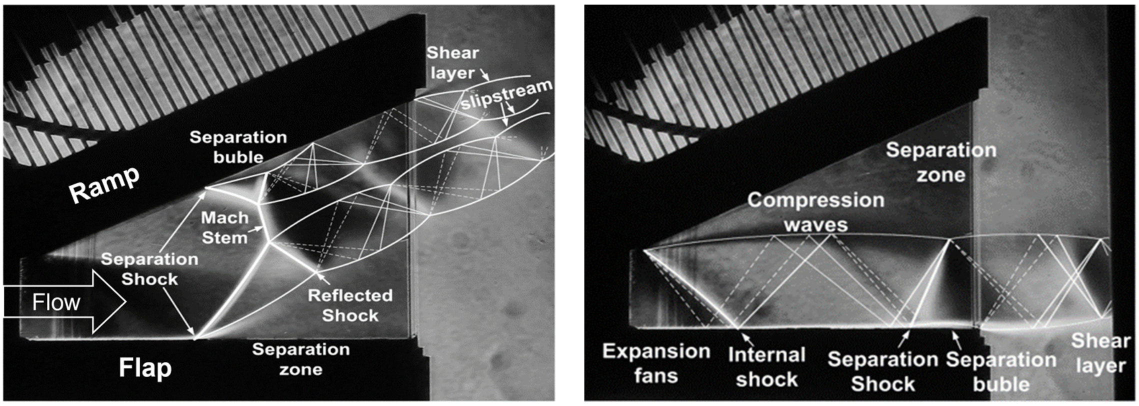

(**a**) (**b**)

Figure 1. Flow separation patterns during SERN shutdown: (**a**) shock wave structure in RSS (ramp) pattern; (**b**) shock wave structure in RSS (flap) pattern.

In view of the problems caused by the nozzle working in the overexpansion state, several early groups [16–19] conducted research on the flow separation prediction, the transition of separation patterns, and the side load of the axisymmetric rocket nozzle, concluding that the primary source of the side load was separation transition. Watanabe et al. [17] found significant side loads in LE-7A experiments, as well as the vulnerability of some experimental components to damage during nozzle startup and shutdown. Since then, an increasing number of papers have been published studying the transition of separation patterns and its effect on nozzle performance [20–22]. Martelli et al. [21] numerically investigated a subscale parabolic overexpanded rocket nozzle and attempted to explain the hysteresis cycle between the separation patterns by analyzing the numerical solutions. He et al. [22] observed an abnormal transition process from no-flow separation at severe overexpansion to RSS and finally to FSS, even at the design condition. In addition, reducing the gas density or mass flow in severely overexpanded conditions leads to a decrease in the adverse pressure gradient across the separation shock or a weaker shock system, exhibiting a strong coupling relationship with flow separation behavior.

The majority of relevant studies were conducted in a static environment; however, the overexpanded separation zone inside the nozzle would interact with the external airflow [23,24]. Mousavi et al. [25] compared the shock wave position at different Mach numbers of the external flow, finding that the shock wave was positioned closer to the nozzle exit at high Mach numbers. Lee et al. [26] numerically studied the flow separation mechanism of a thrust-optimized parabolic nozzle in high-altitude experiments, and the observed flow characteristics showed that the separation pattern and the transition process were very different from those in sea-level experiments. In previous projects conducted by the authors [27,28], the impact of NPR and external Mach numbers on the flow separation patterns of an overexpanded SERN was extensively examined. The results showed that FSS became the most common separation pattern considering the external flow field, which was in contrast to the results under the static state.

The operation of the RBCC engine is governed by the combined effect of the NPR and flight Mach number. Specifically, the acceleration process of aircraft startup entails specific rules regarding the variation process and rate of the flight Mach number. To the authors' knowledge, no research has been carried out on the flow field under the aforementioned conditions and the effect of external flow acceleration on the nozzle performance. Therefore, the work presented in this paper is instructive for investigating the interaction between the internal and external flow of the nozzle.

2. Numerical Simulation Methods and Validation

The test model adopts the asymmetric nozzle shown in Figure 2. The design of the expansion contour is based on the maximum thrust theory. The sketch of the nozzle is shown in Figure 3. The angle at the ramp exit is 0°, the area of the throat (A_t) is 419.9 mm^2, and the aspect ratio of the throat is 2.5. The area of the nozzle exit (A_{exit}) is 1290.58 mm^2, the expansion length is 92 mm, and the contraction length is 30 mm. This model was used to conduct a cold airflow wind tunnel experiment, and the details of the experimental scheme are provided in a previous study [29].

Figure 2. Tested SERN model in the experiment.

The simulation model was a subscale two-dimensional SERN, and the geometry was generated using ICEM v12.0 software with a structured mesh, as shown in Figure 4. The node distributions in the x and y directions of regions 1, 2, 3, 4, 5, and 7 were 80 × 80, 150 × 80, 150 × 80, 120 × 80, 40 × 50, and 150 × 50, respectively. The node distribution of regions 6 and 8 were 120 × 50. The grid described above is defined as the medium one, the grid with double the nodes in the x and y directions is defined as the fine grid, and the mesh with half the nodes is defined as the coarse grid.

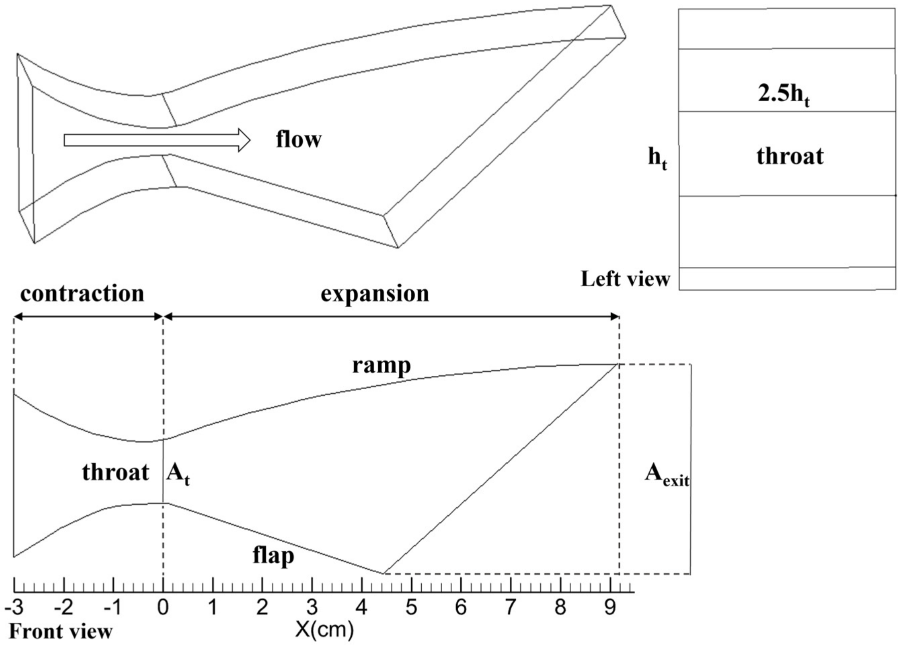

Figure 3. Sketch of the SERN model.

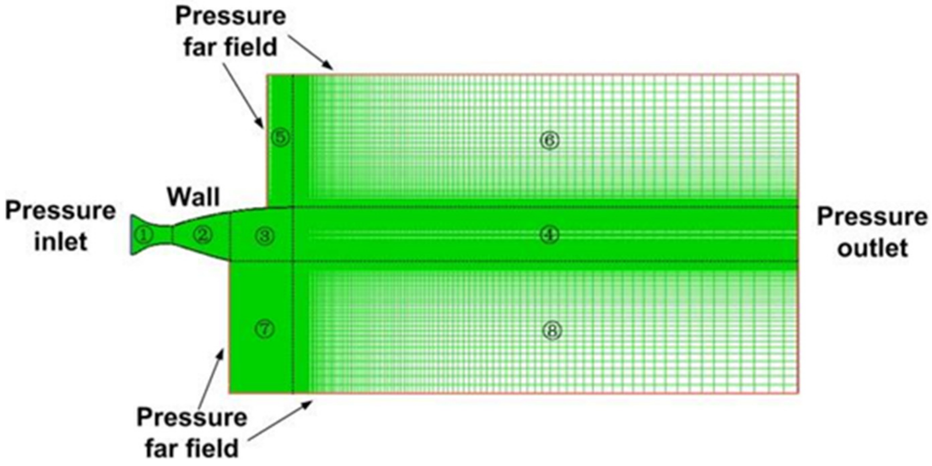

Figure 4. Mesh of the SERN for numerical simulation.

Numerical simulations were carried out using the commercial software FLUENT v12.0, and the two-dimensional Navier–Stokes equations were solved, including the conservation equations for mass, momentum, and energy. In the computational process, the implicit method was used for time advancement to accelerate the convergence. The default Roe-FDS format was used to compute the flux, and the second-order upwind format was used to discretize the control equation. In order to ensure stability and correctness, the Courant number was maintained below 5 in the two-dimensional steady simulation. In the iterative process, the convergence of the computation was assessed by monitoring the mass flow at the inlet and outlet of the nozzle. On the other hand, the residual values of parameters such as the continuity equation, the velocity components, and the energy equation had to be reduced to less than 10^{-4}. The viscous model is the renormalization group (RNG) k–ε model, which is a well-validated turbulence model for predicting the separation flow field of the nozzle [27–30]. The simulation model has the same conditions as the experiment, and the settings are listed in Table 1. Due to the complex flow structure formed by separation and reattachment in SERN, y^+ cannot be controlled in a small range. The y^+ value varied between 10 and 80 in the simulation, thus meeting the requirements of the turbulence model.

Table 1. Settings for numerical simulation.

Property	Setting
Materials	Ideal gas, compressible
Dimensionality	2D
Discretization method	Second-order upwind
Solution method	Density-based solver
Solution formulation	Implicit
Time dependence	Steady
Turbulent model	k-epsilon RNG
Near-wall treatment	Standard wall function
Pressure—inlet	Total pressure = 124,008.5 Pa, temperature = 296.5 K
Pressure—far-field	*Ma* = 0, static pressure = 35,422.69 Pa, temperature = 296.5 K
Pressure—outlet	Total pressure = 35,422.69 Pa, temperature = 296.5 K
Wall	Adiabatic

Figure 5 shows the pressure distribution of the expansion ramp. The horizontal axis was normalized using throat height, while the vertical axis was normalized using the ambient static pressure. The simulations accurately predicted the separation point and reattachment process; however, there was a slight discrepancy in the pressure rates before and after the shock wave. It can be observed from Figure 5 that the fine grid results are in good agreement with those of the medium grid. However, a larger deviation is observed between the results obtained from the coarse grid and the medium grid. At approximately X/ht = 6.4, the maximum relative error between the two grids reached 3%. Thus, the medium grid is suitable for obtaining accurate solutions. Consequently, the medium grid was chosen for subsequent research. Figure 6 presents a comparison between the experimental Schlieren and the numerical results; the CFD method allows for the accurate simulation of the flow-field structure. Simulation data also facilitate the presentation of flow-field details more conveniently.

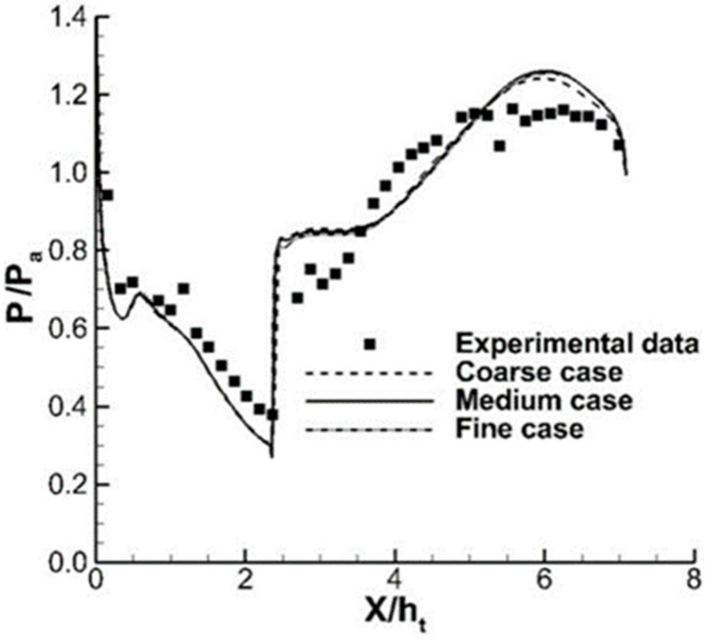

Figure 5. Wall pressure distribution of the expansion ramp.

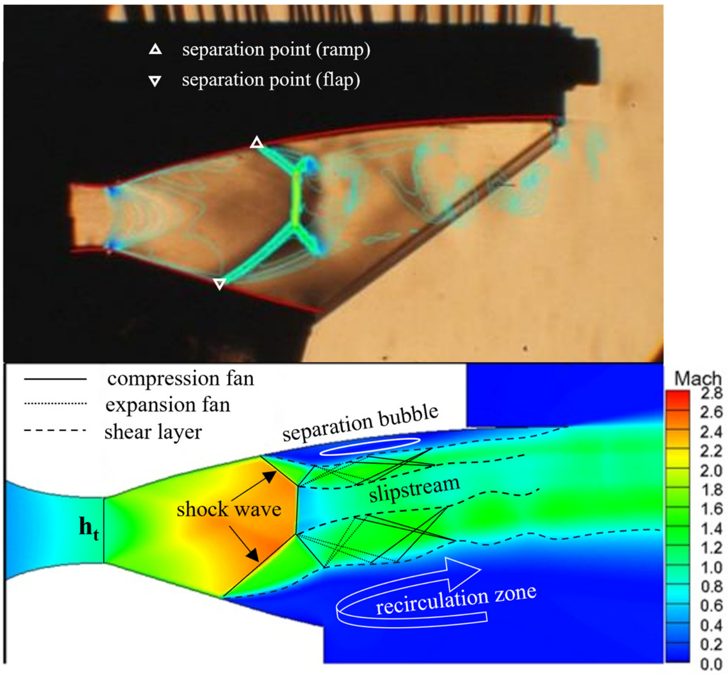

Figure 6. Comparison of the Schlieren image and the CFD results, *NPR* = 3.5.

3. Results and Discussion

3.1. Nozzle Design

The objective of the RBCC is flight within an extremely wide range of Mach numbers, enabling the aircraft to take off from the ground and accelerate to hypersonic cruising states. Throughout this process, there is a significant variation in the operating pressure ratio of the nozzle, which starts at around 2 and increases to over 600. The SERN was designed according to the experimental data of the Glenn Research Center [31] shown in Table 2.

Table 2. Experimental data of RBCC engine.

Ma_∞	Altitude (km)	Ambient Static Pressure, P_a (Pa)	Combustor Total Pressure, P_c* (Pa)	*NPR*
0	0	101,325		
2	8.3	34,061.1	166,899.4	4.9
2.5	11.3	21,781.0	228,700.5	10.5
3	13.6	15,084.1	303,190.4	20.1
4	17.3	8473.5	558,403.6	65.9
5	20.1	5414.4	904,746.2	167.1
6	24.4	2811.0	705,561.0	251
9	28.2	1580.5	1,134,799.0	718
10	31.1	1017.6	1,996,229	1961.7
12	33.5	710.4	3,368,361.6	4741.5

For the Strutjet engine, a previous study [32] demonstrated that the cruise Mach number of the aircraft reaches 8. In order to take into account the low-Mach number performance at ramjet takeover and Mach 8 cruise state, the nozzle optimization was selected at Mach 6. When operating in injection mode or subsonic-combustion ramjet mode, the RBCC engine with fixed geometry construction lacks a contraction section in the nozzle that facilitates the acceleration of the airflow to sonic speed. Therefore, the throat serves as the nozzle inlet. The thermal throat is formed through organized combustion, and the number of the airflow reaches 1 via heat injection. However, the combustion chamber channel usually has an expansion angle, which makes the inlet Mach number of the nozzle slightly larger than 1. When the RBCC operates in supersonic-combustion ramjet (scramjet) mode, the airflow Mach number before the nozzle inlet may reach 2 or higher [33].

Assuming no chemical reaction occurs within the nozzle channel, the wall of the nozzle is adiabatic, and the total pressure loss is ignored; thus, $P_{in}{}^* = P_{exit}{}^*$, $T_{in}{}^* = T_{exit}{}^*$.

According to the flow conservation relationship, the following equations can be obtained:

$$K_{in}\frac{P_{in}{}^*}{\sqrt{T_{in}{}^*}}q(Ma_{in})A_{in} = K_{exit}\frac{P_{exit}{}^*}{\sqrt{T_{exit}{}^*}}q(Ma_{exit})A_{exit} \tag{1}$$

$$K = \left(\frac{\gamma}{R}\right)^{\frac{1}{2}}\left(\frac{2}{\gamma+1}\right)^{\frac{\gamma+1}{2(\gamma-1)}} \tag{2}$$

$$q(Ma) = Ma\left[\frac{2}{\gamma+1}\left(1+\frac{\gamma-1}{2}Ma^2\right)\right]^{-\frac{\gamma+1}{2(\gamma-1)}} \tag{3}$$

where * denotes the stagnation flow parameters; subscripts *in* and *exit* represent the nozzle inlet and outlet, respectively; A is the local area; R is the gas constant; and γ is the specific heat ratio of the gas.

The design *NPR* of the nozzle was determined as follows:

$$NPR_{design} = \frac{P_{in}{}^*}{P_{exit}} = \frac{P^*_{exit}}{P_{exit}} = \left(1-\frac{\gamma_{exit}-1}{2}Ma^2_{exit}\right)^{\frac{\gamma_{exit}}{\gamma_{exit}-1}} \tag{4}$$

Using the data in Table 1, and ignoring combustion in the nozzle and changes in the specific heat ratios of the inlet and outlet, a relationship between the area ratio of the nozzle outlet to the inlet and the inlet Mach number was established for each design NPR, as illustrated in Figure 7.

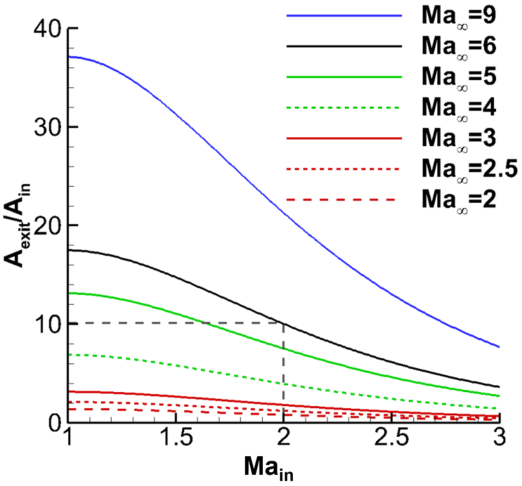

Figure 7. The link between the design area ratio of SERN and the inlet Mach number under various flying situations.

For the Strutjet engine, the working Mach number of 2.5–6 is the subsonic-combustion ramjet mode, and the working Mach number of over 6 is the scramjet mode. When the engine is in the subsonic-combustion ramjet mode, it has a thermal throat, and the Mach number of the nozzle inlet is approximately 1. During the design process, it was considered that the scramjet mode occurred at Mach 6. When the Mach number of the nozzle inlet was 2, the design area ratio was 10.01. Again, for the subsonic-combustion ramjet mode, the nozzle with the area ratio of 10.01 was under-expanded at Mach 5 operation, whereas it was slightly overexpanded at Mach 4 operation and significantly overexpanded below Mach 3. To achieve the desired performance at low speed, the nozzle's design Mach number was 6, and the design area ratio was 10.01. Additionally, the performance of the cruising state with Mach 8 should be considered, and the NPR under this circumstance was determined using the interpolation method. Finally, the nozzle was designed using the maximum thrust theory, with a design NPR of 562.3, corresponding to the operating state of Mach 8. After obtaining the profile, it was truncated according to the condition that the area ratio of outlet to inlet was 10.01, and the resulting nozzle profile is displayed in Figure 8. Table 3 details the specific design parameters for the maximum thrust nozzle.

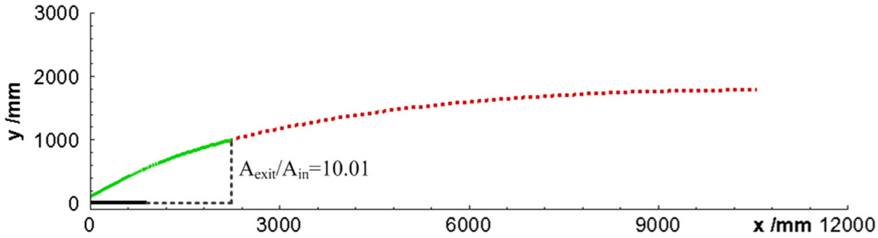

Figure 8. The designed profile of the minimum length of the nozzle for Mach 8.

Table 3. Specific design parameters of maximum thrust nozzle profile at Mach 8.

Design Parameters	Value
Total pressure of the inlet P_D* (Pa)	888,732.02
Total temperature of the inlet T_D* (K)	2000
Static pressure of the inlet P_D (Pa)	115,250.77
Ambient pressure P_a (Pa)	1580.53
Height of inlet h_t (mm)	100
The ratio of specific heat γ	1.33

The thrust coefficient is defined with a surplus impulse of the nozzle outlet as follows:

$$\text{Thrust confficient} = \frac{\text{actual surplus impulse of nozzle outlet}}{\text{ideal surplus impulse of nozzle outlet}} \tag{5}$$

The surplus impulse function is expressed as follows:

$$I = \dot{m}v + A(p - p_a) \tag{6}$$

where $\dot{m}$ denotes the mass flow rate.

As seen in Table 4, the nozzle maintained a high level of thrust performance under the Mach numbers of 4–9.

Table 4. Thrust coefficient of the nozzle under different Mach number flight conditions.

Flight Mach Numbers	Thrust Coefficient
3	0.8011
4	0.9636
5	0.9784
6	0.9770
8	0.9747
9	0.9725

When the Mach number was <3, the thrust performance of the nozzle was poor. Particularly, when the Mach number <2, due to the actual area ratio of the nozzle outlet to inlet being too large, the gas in the nozzle experienced severe overexpansion, and the positive impulse could not be obtained at the nozzle outlet, preventing the nozzle from producing effective thrust. When the Mach numbers were in the range of 0–3, however, the RBCC engine operated in the rocket injection mode, and partial thrust could be provided via the rocket to compensate for the loss caused by the overexpansion state.

3.2. Simplified Acceleration Process

There were also different separation flow fields for the designed SERN in the severe overexpansion state, and the transition of separation patterns occurred under changing conditions. Figure 9 shows the Mach contour of the flow field under various working NPRs at sea level. As can be seen, the airflow in the nozzle was along the expansion ramp, resulting in RSS (ramp); there was no FSS or RSS (flap). Thus, the sea level condition with only a change in NPR did not cause a transition of the flow separation pattern in the nozzle.

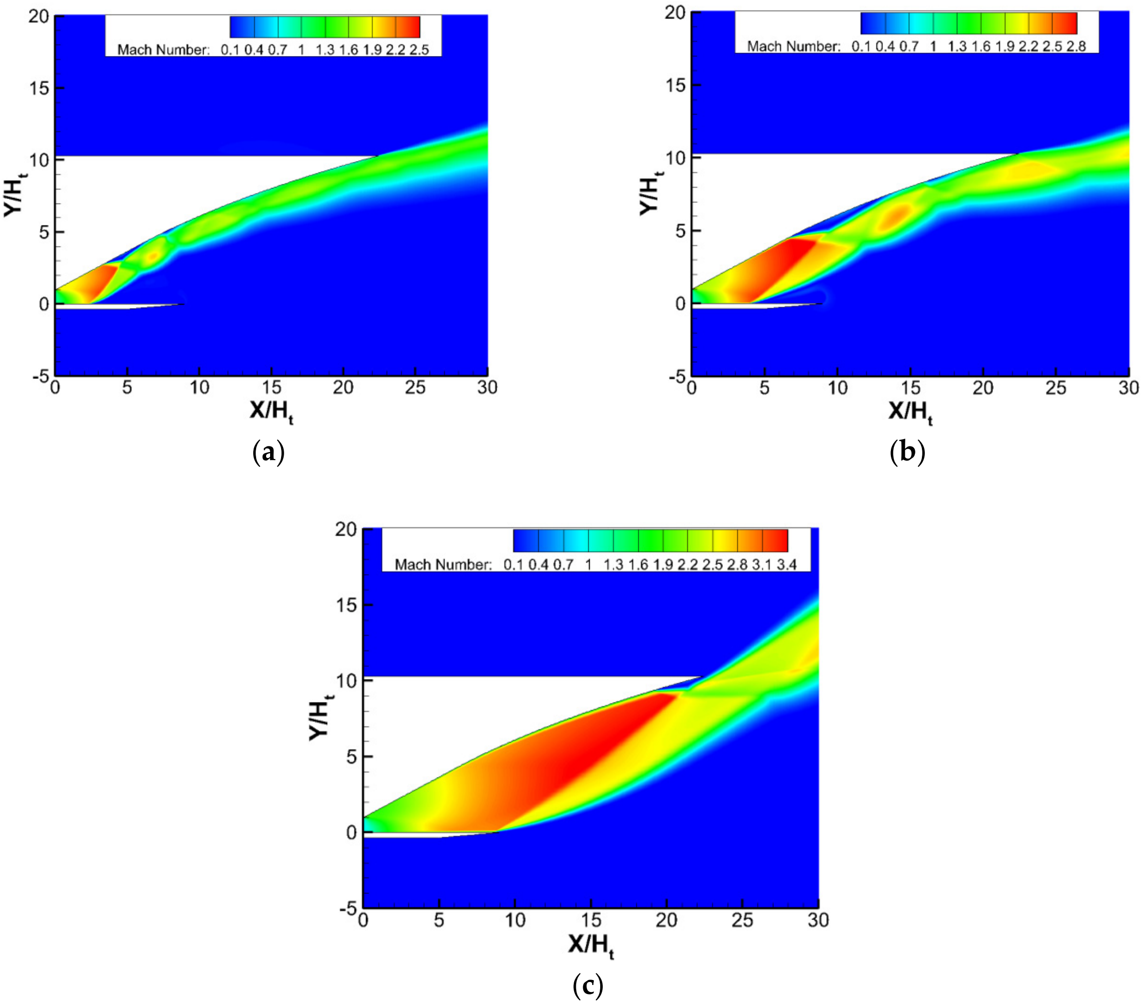

(**a**) (**b**) (**c**)

Figure 9. Mach contours of the flow field under different *NPR*, *Ma* = 0: (**a**) *NPR* = 4.9; (**b**) *NPR* = 10.5; (**c**) *NPR* = 20.1.

Figure 10 provides the Mach contours of the flow field under real flight conditions. As can be seen, the nozzle exhibits FSS pattern under conditions (a) and (b), and there is no separation on the flap but a tail shock. Under condition (c), the shock wave on the flap does not shoot to the ramp and hence does not induce the formation of separation shock wave and separation bubble there. If the aircraft takes off from the ground and accelerates, RSS (ramp) and FSS separation patterns appear sequentially in the nozzle, accompanied by the corresponding transition of the separation patterns.

The simplified acceleration process was simulated under the condition that the variation rate of Mach number was 1/s, and the results are shown in Figure 11. With the increase in external Mach number, the separation shock wave on the flap steadily moved backward, compressing the flap recirculation zone. The separation shock on the flap rapidly moved to the trailing edge until the jet shear layer interacted with the boundary of outflow, as illustrated in Figure 11b. Subsequently, the jet deflected downward, the flap recirculation zone disappeared, and the separation bubble on the ramp expanded, forming a large recirculation zone. The ambient gas gradually entered the recirculation zone, and the separation shock on the ramp moved forward to the nozzle inlet. As illustrated in Figure 11c, the lower shear layer of the jet fully interacted with the outflow to form a slipstream. Finally, as shown in Figure 11d, the flow field remained steady, and the transition process was completed.

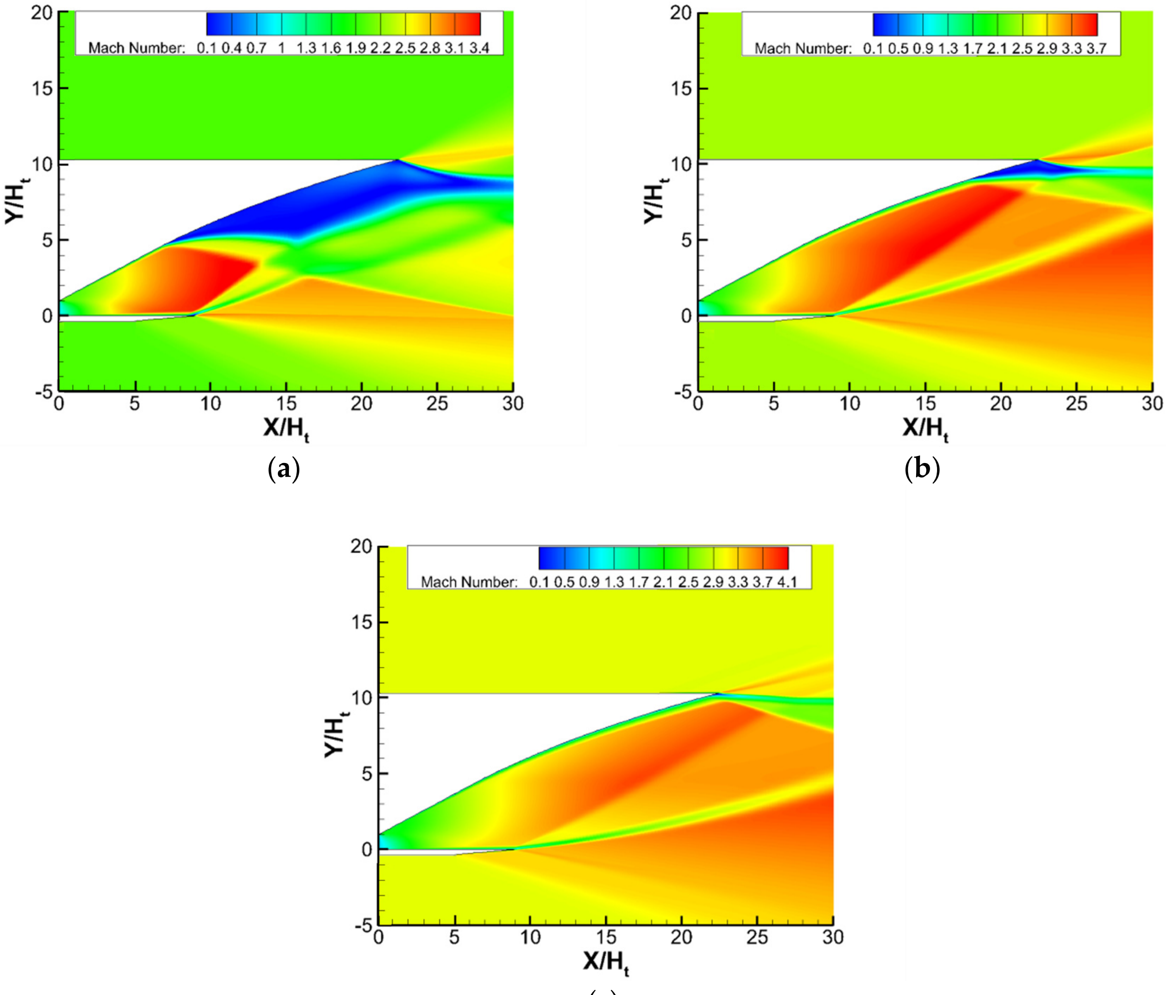

(**a**) (**b**)

(**c**)

Figure 10. Mach contour of the flow field under different flight conditions: (**a**) *NPR* = 4.9, *Ma* = 2.0; (**b**) *NPR* = 10.5, *Ma* = 2.5; (**c**) *NPR* = 20.1, *Ma* = 3.0.

Figure 12 illustrates the fluctuation in nozzle performance during the transition process. The thrust, lift, and moments are nondimensionalized using the initial values. Significant alterations occurred in these parameters during the transition. At the peak of the performance degradation, the decreases in thrust, lift, and moments were 11.8%, 31.27%, and 37.30%, respectively. Upon completion of the transition, the decreases in thrust, lift, and moments were 5.56%, 15.93%, and 26.65%, respectively.

The above results verify that the transition of separation patterns will occur in the SERN during startup and acceleration, but the real flight conditions of the RBCC engine are complex. The interactions between the external flow and the jet, the recirculation zone, and the boundary layer are critical during the transition process induced by external Mach number. Different accelerations can have an effect on the Mach number of the airflow at the nozzle exit, hence altering the transition process.

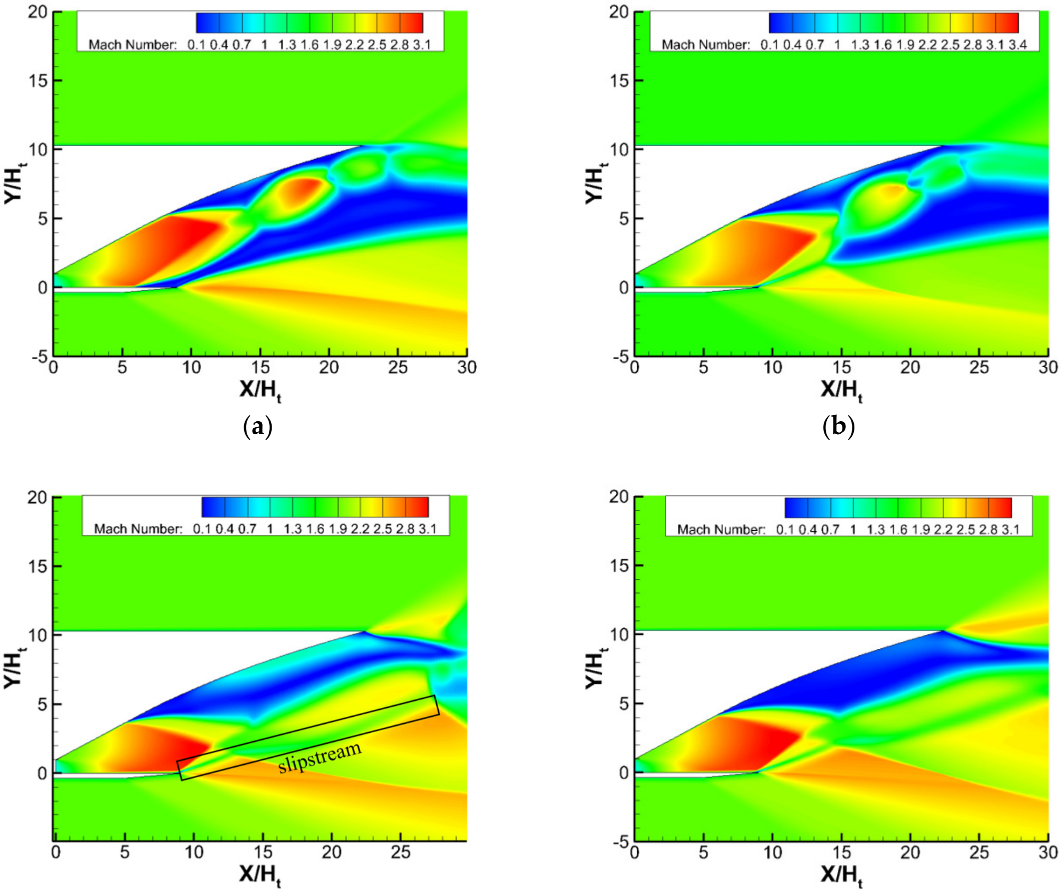

(**a**) (**b**)

(**c**) (**d**)

Figure 11. The transition from RSS (ramp) to FSS during the acceleration process: (**a**) t_0, Ma = 1.86; (**b**) t_0 + 0.004 s, Ma = 1.864; (**c**) t_0 + 0.009 s, Ma = 1.869; (**d**) t_0 + 0.02 s, Ma = 1.88.

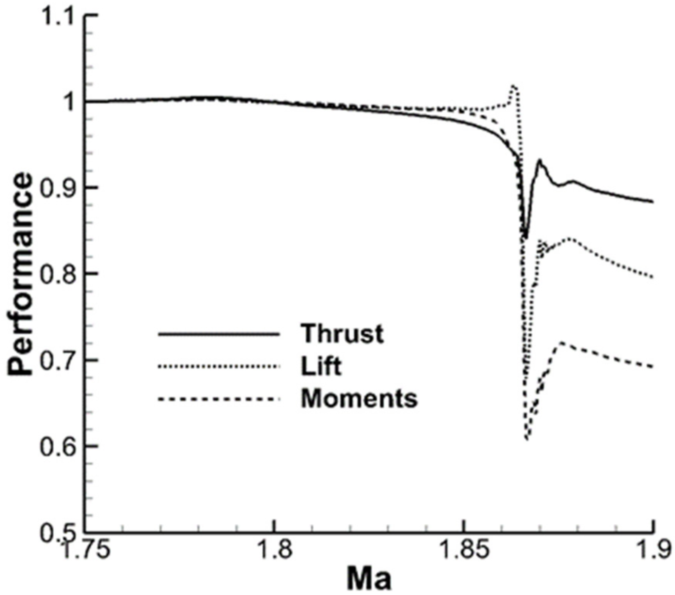

Figure 12. Variation in nozzle performance during the transition from RSS (ramp) to FSS.

3.3. *Effect of Acceleration*

The numerical simulation results with external Mach number increase rates of 0.2/s, 0.5/s, 1/s, and 2/s are chosen for discussion. When the rate is 0.2/s, it is close to the real flight situation of the RBCC engine. The transition from RSS (ramp) to FSS was simulated with an initial external Mach number of 1.75 and NPR of 4.9.

Figure 13 demonstrates the relationship between nozzle thrust and Mach number for different increase rates of Mach number. Meanwhile, to explore the influence of the Mach number change rate on the transition duration, the minimum thrust points under Mach number increase rates of 0.5/s, 1/s, and 2/s are adjusted to coincide with the point of 0.2/s case, and the time at these points is marked as t_0, as shown in Figure 14. According to the analysis of the results, RSS (ramp)–FSS transition occurred under the four cases, indicating that the external Mach number variation rate did not affect the principle of the separation flow field and had a negligible effect on the duration of the transition process. With an increase in the Mach number, the critical Mach number corresponding to the transition points also gradually increased, and the variation in peak thrust during the transition process similarly increased.

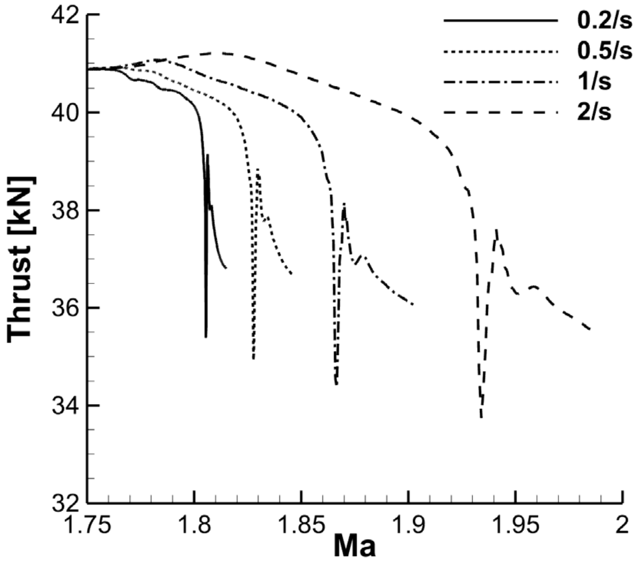

Figure 13. Variation in the nozzle thrust with Mach number for different increase rates of Mach number.

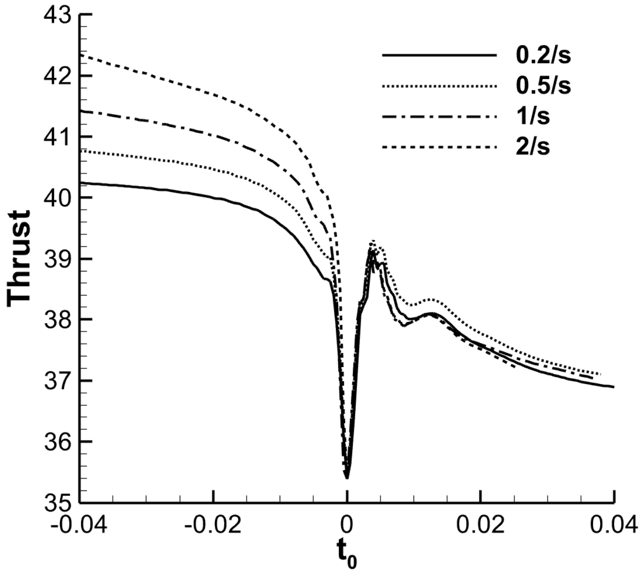

Figure 14. Variation in nozzle thrust with time for different increase rates of Mach number, after an adjustment.

To further discuss the influence of the external Mach number change rate, the constant Mach number contour and constant pressure contour for the flow field at an external Mach number of 1.8 are presented in Figures 15 and 16. Among the four simulated cases, apart from the varying rate of change in the external Mach number, all other settings remained identical. Due to the acceleration of the flight, the external flow field underwent an airflow accumulation process, that is, when the fluid with a lower Mach number had not yet completely flown through the outer wall of the aircraft, the gas with a higher Mach number began to enter the computational domain. Consequently, a higher rate of change in the external Mach number led to a more pronounced accumulation effect in the external flow field, indicating that the aircraft accelerated to a higher Mach number condition while the Mach number at the nozzle exit remained comparatively low. As a result, the faster the change in the Mach number, the more noticeable the effect of external flow-field accumulation.

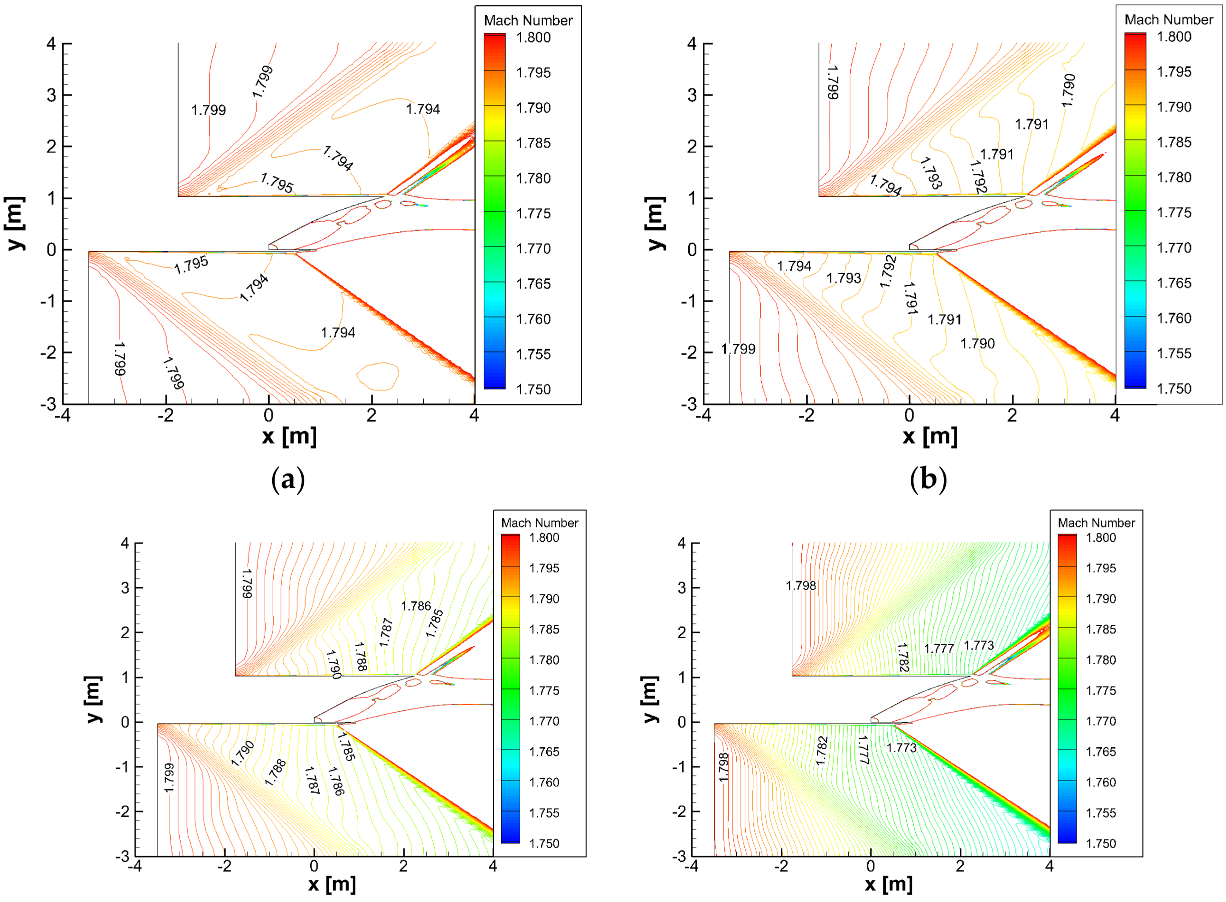

(**a**) (**b**)

(**c**) (**d**)

Figure 15. Constant Mach number contour at Mach 1.8 with different increase rates of Mach number: (**a**) 0.2/s; (**b**) 0.5/s; (**c**) 1/s; (**d**) 2/s.

These cases simulated the process of accelerated flight at a specific altitude, where the boundary static pressure remained constant. However, due to the accumulation of airflow, the gas with a higher Mach number upstream exerted a certain compressive effect on the gas with a lower Mach number downstream. Combined with observations from Figure 16, it can be inferred that a higher rate of change in the external Mach number led to a more pronounced compressive effect, resulting in higher static pressure at the nozzle exit. Consequently, the actual nozzle pressure ratio decreased, which contributed to delaying the transition of separation patterns.

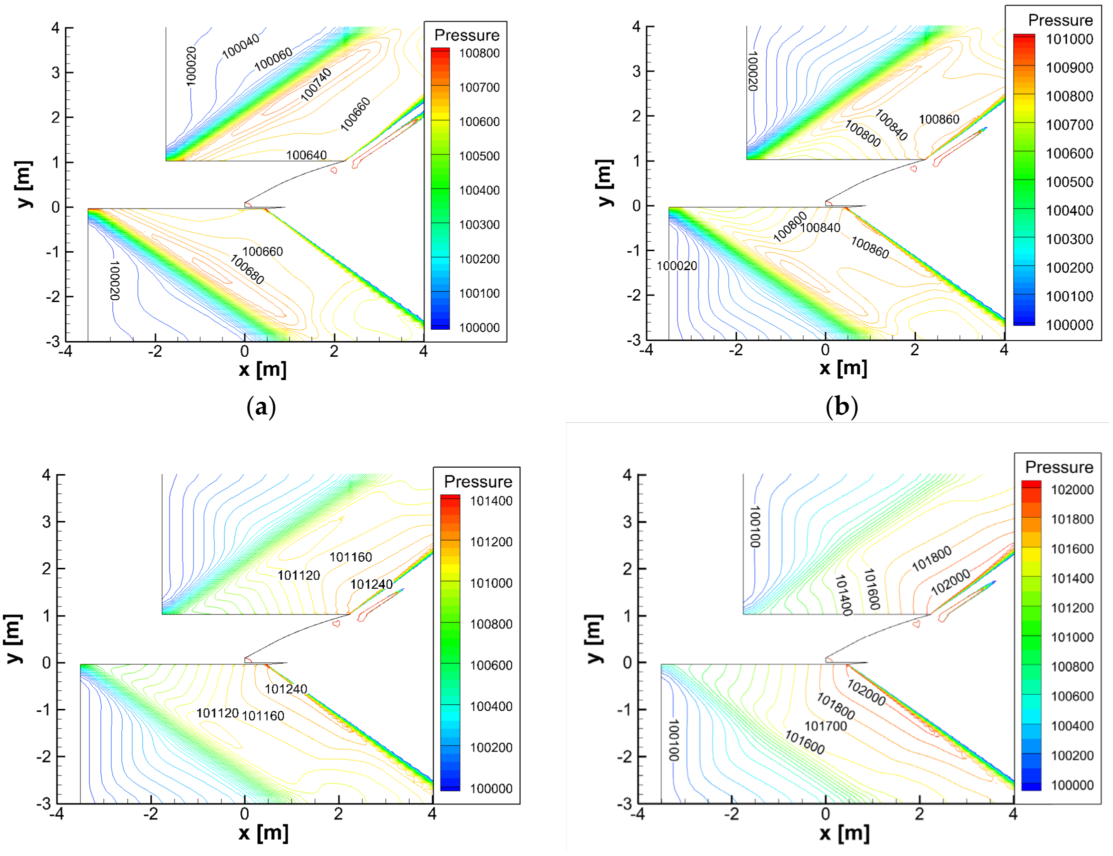

(**a**) (**b**) (**c**) (**d**)

Figure 16. Constant pressure contour at Mach 1.8 with different increase rates of Mach number: (**a**) 0.2/s; (**b**) 0.5/s; (**c**) 1/s; (**d**) 2/s.

3.4. Real Take-off Acceleration Process

RBCC-powered booster aircraft typically follow a two-stage trajectory: inconstant dynamic pressure climbing and constant dynamic pressure climbing. The separation pattern transition phenomena of the nozzle during take-off acceleration were explored in this work using the booster trajectory design of Xue et al. [34]. During the take-off phase, the aircraft flew along a direct ascending path, reaching the flight condition Mach 3.5 and achieving ideal dynamic pressure in the ramjet mode of the RBCC engine. The airplane then began climbing in the direction of the constant dynamic pressure path. Understanding the link between flight altitude and Mach number is required to determine the environmental parameters and obtain the boundary conditions for the nozzle flow separation pattern transition simulations. Figure 17 illustrates the relationship between the Mach number and the flight altitude with flight time in a direct ascending path.

The method described in ISO 2533—Standard Atmosphere (1975) was used to calculate the ambient gas parameters. Static pressure in the environment is expressed as follows:

$$p = \begin{cases} 100 \times (3.731444 - 8.41728H)^{5.25588}, -1450 < H \leq 11000\text{m} \\ 100 \times 226.32 \times \exp(1.7345737 - 1.5768852 \times 10^{-4}H), 11000 < H \leq 20000\text{m} \\ 100 \times (1.2386515/(1 + 5.085177 \times 10^{-6}H))^{34.16321878}, 20000 < H \leq 32000\text{m} \\ 100 \times (1.9630052/(1 + 2.013364 \times 10^{-5}H))^{12.20114957}, 32000 < H \leq 47000\text{m} \end{cases} \tag{7}$$

Ambient temperature is expressed as follows:

$$T = \begin{cases} 301.15 - 6.5 \times (H - 2), -2 < H \leq 0\text{km} \\ 288.15 - 6.5H, 0 < H \leq 11\text{km} \\ 216.65, 11 < H \leq 20\text{km} \\ 216.65 + (H - 20), 20 < H \leq 32\text{km} \\ 228.65 + 2.8 \times (H - 32), 32 < H \leq 47\text{km} \end{cases} \tag{8}$$

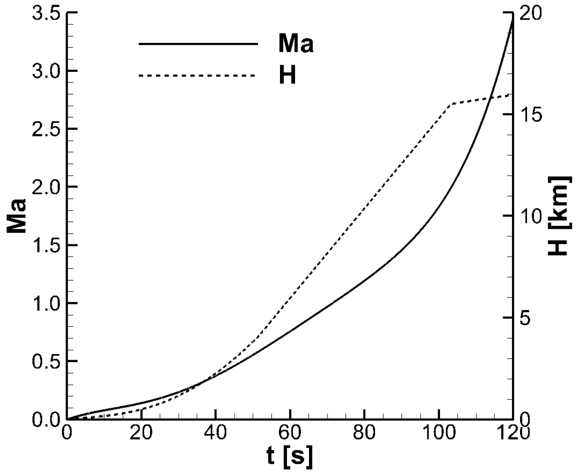

Figure 17. Relationship between the Mach number and the flight altitude with flight time in a direct ascending path.

The boundary conditions in the numerical simulation were set in accordance with the relationship between the Mach number and NPRs shown in Table 2. When the Mach number $\leq$ 2, the given NPR = 4.9; when 2 < Mach number < 2.5, the NPR increased linearly from 4.9 to 10.5; when 2.5 < Mach number $\leq$ 3, the NPR increased linearly from 10.5 to 20.1; and when 3 < Mach number $\leq$ 4, the NPR increased linearly from 20.1 to 65.9. When the flight Mach number $\leq$ 3.5, the operational modes of the RBCC were the injection mode or subsonic-combustion ramjet mode, with the nozzle inlet Mach numbers around 1. During the numerical simulation, the influence of nonuniform parameters at the nozzle inlet was neglected. Instead, a uniform inlet condition with Mach number = 1 was imposed using far-field boundary conditions, while other boundary conditions were varied using user-defined functions (UDFs). The computational process began with an external Mach number of 0.1 and continued until there was no flow separation inside the nozzle. As illustrated in Figure 17, the Mach number change rate was slow throughout the actual ascending phase, ranging from 0.02/s to 0.03/s. In the simulation process, the Mach number change rate increased by 50 times due to the consideration of the computational amount, resulting in a Mach number change rate of approximately 1/s.

As illustrated in Figure 18, the nozzle performance curve exhibits a declining tendency during the direct ascending path and then begins to climb at approximately Mach 2.5. The Mach contours of the nozzle flow field with external Mach numbers of 0.5, 1.0, 1.5, and 2.0 are shown in Figure 19. According to the presented flow fields, when Mach number < 2, the nozzle entered RSS (ramp) mode, and as the external Mach number increased, the separation points on the ramp and flap steadily moved backward, away from the nozzle inlet. When the external Mach number was small, the design NPR was high, and its actual working NPR was relatively low, the separation points of the upper and lower walls were close to the throat and distant from the trailing edge of the nozzle. As a result, there is considerable room for airflow development after the separation point, and the RSS (ramp) pattern continues to be observed in the flow field of the nozzle over a broad Mach number range.

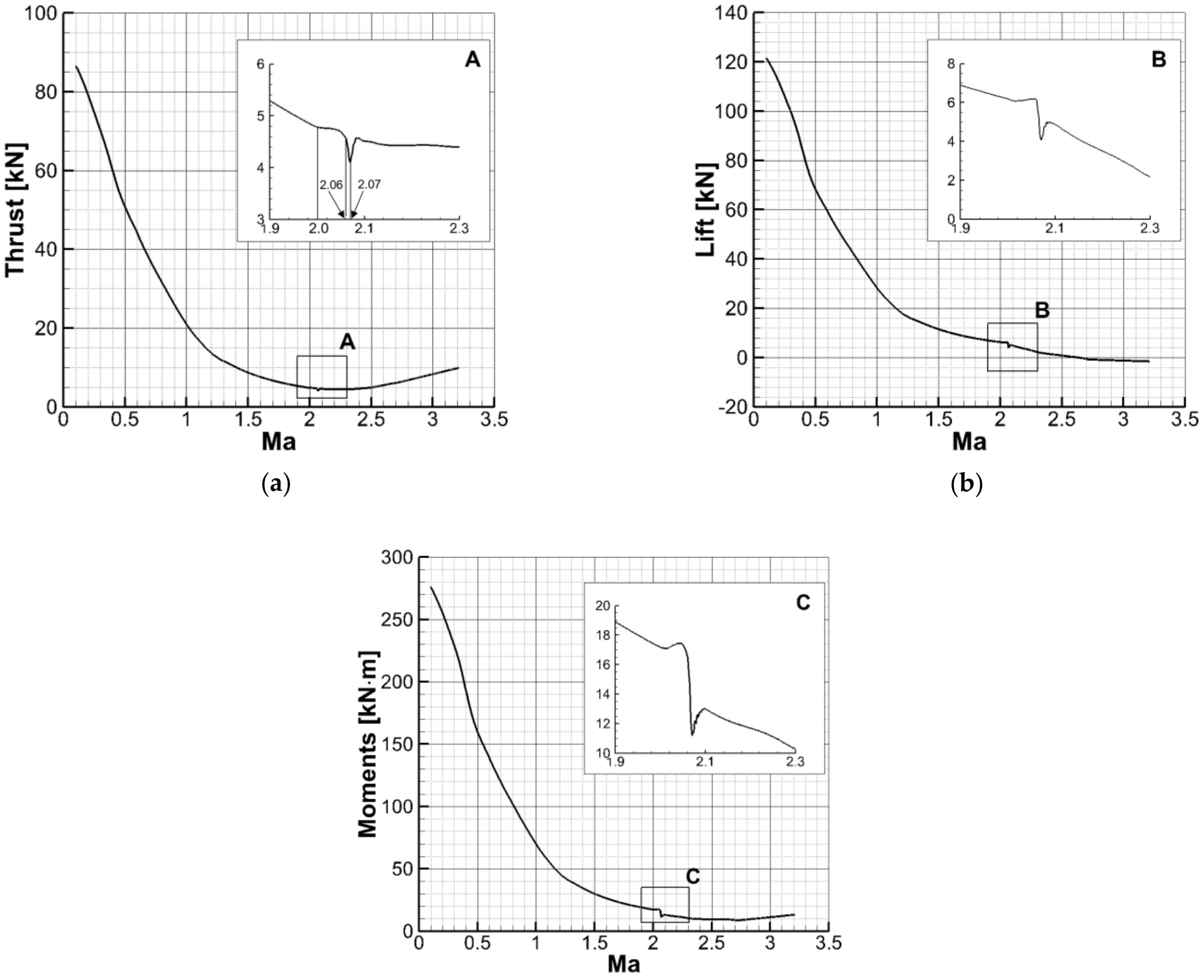

(**a**)

(**b**)

(**c**)

Figure 18. Variation in the nozzle performance with Mach number in the direct ascending path: (**a**) thrust; (**b**) lift; (**c**) moments.

In addition, a dramatic change can be clearly detected on the performance curve, corresponding to the separation pattern transition from RSS (ramp) to FSS depicted in Figure 20. Although the flow-field variation in the separation pattern transition process is comparable to that in the linearly increasing Mach number seen in Figure 11, the critical Mach numbers of the two transition processes are considerably different.

As demonstrated in Figures 19 and 20, during the transition process from RSS (ramp) to FSS, the flap separation shock rapidly moved toward the trailing edge, followed by a subsequent downward deflection of the jet, resulting in drastic changes in the flow field. After the transition from RSS (ramp) to FSS, a larger recirculation zone remained on the expansion ramp, as shown in Figure 21a. As the external Mach number increased, the separation shock on the expansion ramp continued to move downstream, suggesting the possibility of a similar phenomenon, where the ramp separation shock rapidly moved toward the trailing edge, causing significant changes in the flow-field structure. However, as illustrated in Figure 18, there is a continuous and smooth change in the nozzle following the RSS (ramp)–FSS transition process, with no mutation. Figure 21 depicts the process through which the flow field changed following the transition from RSS (ramp) to FSS. As the external Mach number increased, the separation shock wave on the ramp gradually moved downstream, compressing the recirculation zone until it disappeared. Throughout the process, no flow separation occurred.

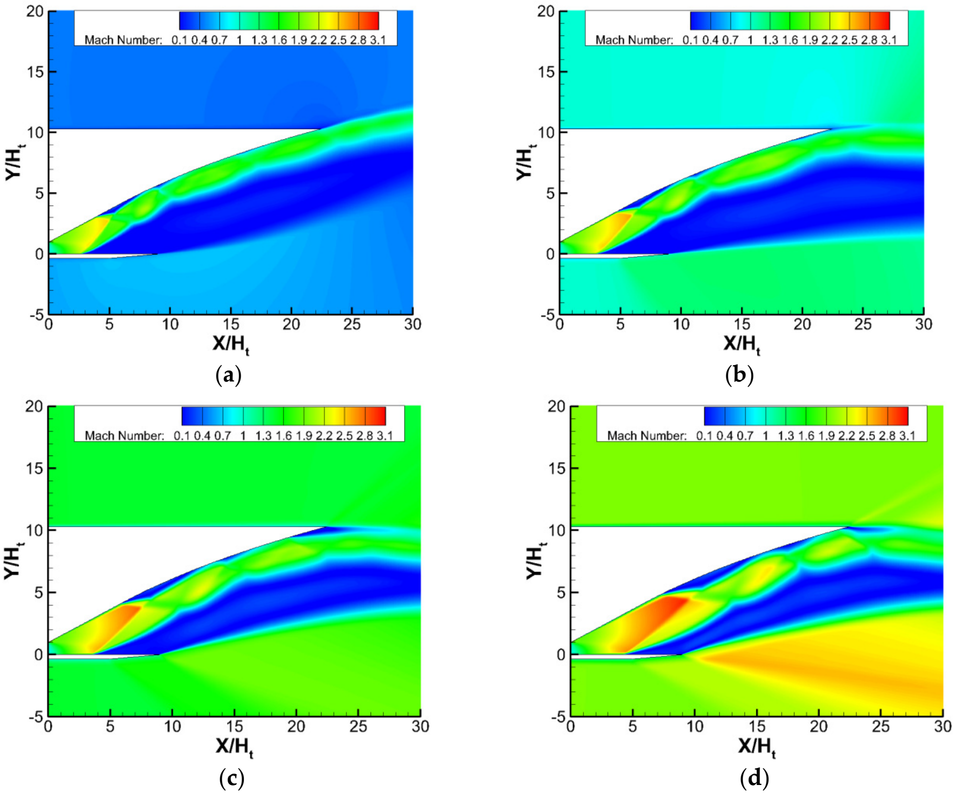

(**a**) (**b**)

(**c**) (**d**)

Figure 19. Mach contour of the flow field in RSS (ramp) at different Mach numbers: (**a**) *Ma* = 0.5; (**b**) *Ma* = 1.0, (**c**) *Ma* = 1.5; (**d**) *Ma* = 2.0.

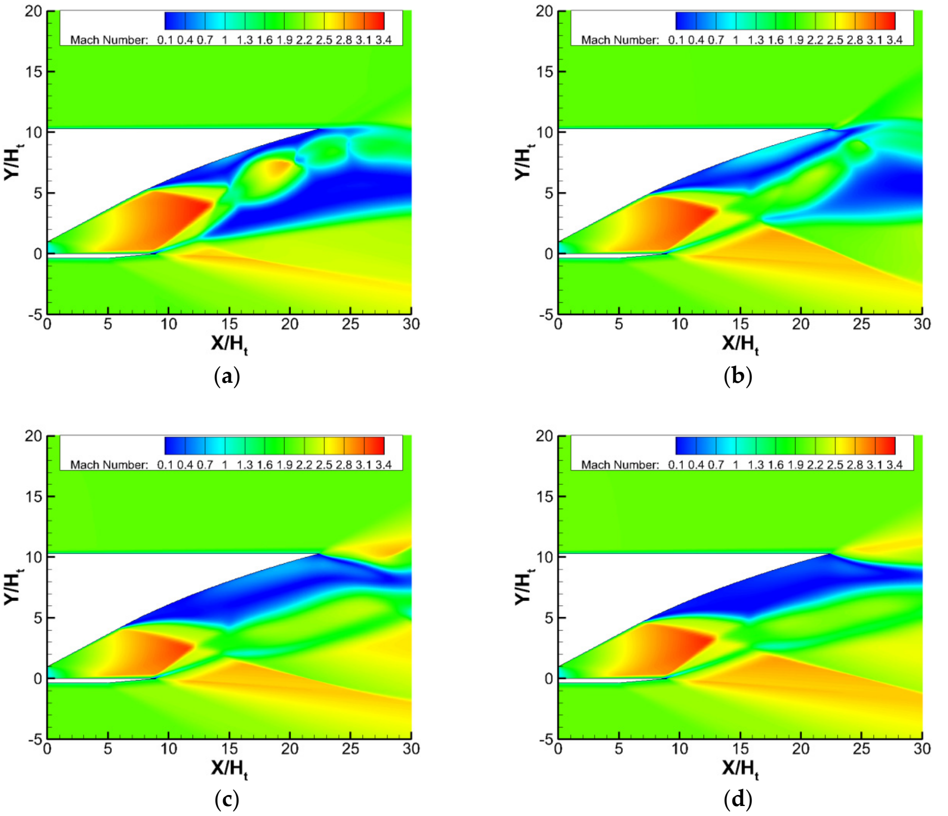

(**a**) (**b**)

(**c**) (**d**)

Figure 20. The transition from RSS (ramp) to FSS in the direct rising path: (**a**) t_0, *Ma* = 2.0606; (**b**) t_0 + 0.003 s, *Ma* = 2.0693; (**c**) t_0 + 0.008 s, *Ma* = 2.0840; (**d**) t_0 + 0.015 s, *Ma* = 2.1048.

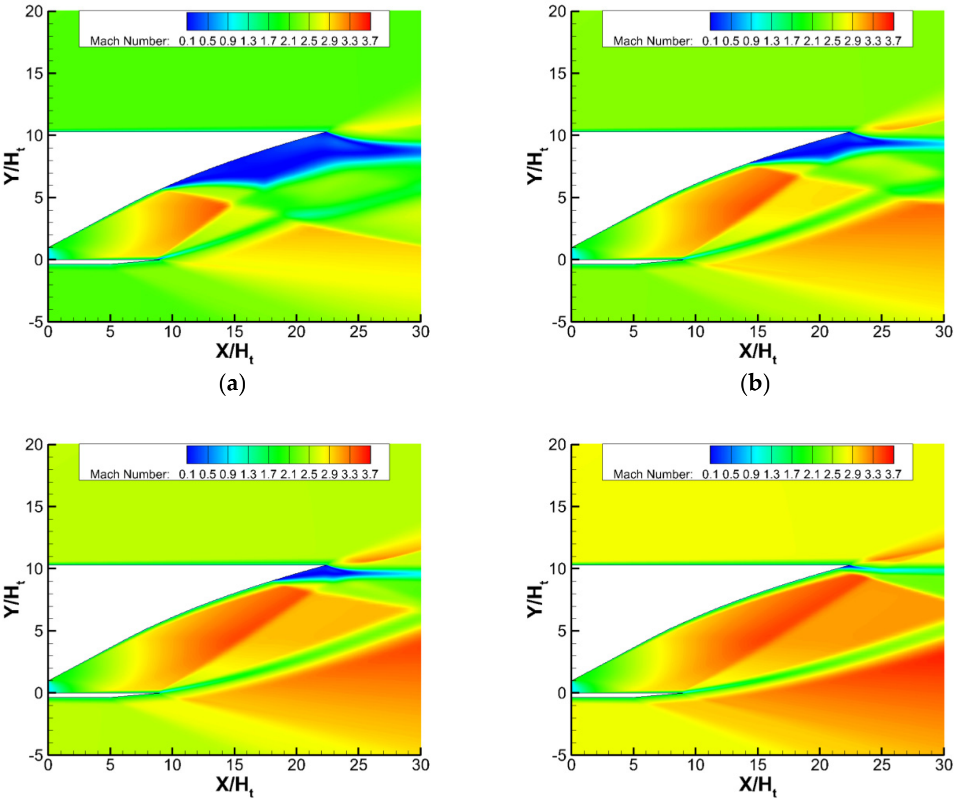

(**a**) (**b**)

(**c**) (**d**)

Figure 21. Variation in the flow field during the transition from FSS to no-flow separation pattern: (**a**) *Ma* = 2.2; (**b**) *Ma* = 2.4; (**c**) *Ma* = 2.6; (**d**) *Ma* = 2.8.

In comparison to the transition from RSS (ramp) to FSS, the transition from FSS to a no-flow separation pattern did not result in a performance mutation. First, the recirculation zone on the expanded ramp in FSS was larger than that on the flap in RSS (ramp). Environmental flow entered the ramp recirculation zone more smoothly, allowing the zone to develop more steadily as well. Second, tail shock on the flap severely restricted the development of the separation shock at the expansion ramp when the external Mach number was high, as did the expansion of the recirculation zone, and the effect became more pronounced as the external Mach number increased. Due to the acceleration effect of outflow passing through the flap cowl, with the increase in flight Mach, the tail shock here gradually deflected downward and eventually stopped, which caused flow separation on the ramp, thus ensuring a stable transition process.

4. Conclusions

In this paper, considering the low-Mach number performance at ramjet takeover and the Mach 8 cruise state, the nozzle optimization design was considered to be at Mach 6. Through the numerical method, the flow separation pattern transition processes under the circumstances of linear change in the external Mach number and the real trajectory were simulated. Detailed analyses were carried out for the processes to further understand the influence of changes in the external flow field on the flow field inside the nozzle. The results are as follows:

(1) The external flow Mach number had a significant effect on the overexpansion flow field of the RBCC nozzle. With an increase in the external Mach number, sequential transitions of RSS (ramp) to FSS and FSS to no-flow separation pattern occurred.
(2) The transition principle of the flow separation patterns in the real ascending path was similar to the case with external flow varying linearly, but the Mach number corre-

sponding to the transition points was considerably different. The variation rate of the external Mach number affected the nozzle performance during the transition process.

(3) The higher the variation rate of the external flow Mach number, the more obvious the airflow accumulation effect of the external flow field, which caused an increase in the static pressure at the outlet and a decrease in the real nozzle pressure ratio, delaying the transition of flow separation patterns.

Author Contributions: Conceptualization, Y.Y. (Yang Yu); methodology, Y.Y. (Yang Yu); software, Y.Y. (Yang Yu) and Y.M.; investigation, Y.Y. (Yang Yu), Y.M. and T.Y.; resources, Y.Y. (Yang Yu); writing—original draft preparation, Y.Y. (Yang Yu); writing—review and editing, Y.M., T.Y., Y.Y. (Yalin Yang), S.X. and S.L. All authors have read and agreed to the published version of the manuscript.

Funding: This research was funded by the National Natural Science Foundation of China under Grant No. 11802124, the Jiangsu Province Key Laboratory of Aerospace Power System Foundations (CEPE2020003), and the National Natural Science Foundation of Chongqing (cstc2021jcyj-msxmX1120).

Data Availability Statement: Some or all data, models, or codes generated or used during this study are available from the corresponding author upon reasonable request.

Conflicts of Interest: The authors declare no conflict of interest.

Nomenclature

SERN	Single-expansion ramp nozzle
RBCC	Rocket-based combined cycle
CFD	Computational fluid dynamics
RSS	Restricted shock separation
RSS (ramp)	Restricted shock separation with separation bubble forming on the ramp
RSS (flap)	Restricted shock separation with separation bubble forming on the flap
FSS	Free shock separation
SWBLI	Shock wave/boundary layer interaction
NPR	Nozzle pressure ratio
UDF	User-defined functions
A_t	Area of the nozzle throat
A_{in}	Area of the nozzle inlet
A_{exit}	Area of the nozzle exit
P_a	Ambient pressure
P^*	Total pressure
h_t	Height of the nozzle throat
Ma_∞	Mach number of freestream
Ma_{in}	Mach number of nozzle inlet

References

1. Shi, L.; Yang, Y.; Yang, X.; Zhao, G.; Chen, F.; He, G. Start Limits and Positive Control of RBCC Inlet. *J. Aerosp. Eng.* **2022**, *35*, 04021128. [CrossRef]
2. Wang, Y.; Zhang, Q.; Tang, Z.; Tian, Z.; Zheng, Y. Integrated Thermal Protection System Design for Hypersonic Vehicle Based on New Thermal–Mechanical Method. *J. Aerosp. Eng.* **2022**, *35*, 04021121. [CrossRef]
3. Hiraiwa, T.; Ito, K.; Sato, S.; Ueda, S.; Tani, K.; Tomioka, S.; Kanda, T. Recent Progress in Scramjet/Combined Cycle Engines at JAXA, Kakuda Space Center. *Acta Astronaut.* **2008**, *63*, 565–574. [CrossRef]
4. Gronland, T.; Berens, T. Nozzle/Afterbody Integration of Hypersonic Vehicles by Means of Secondary Air Injection. In Proceedings of the International Aerospace Planes and Hypersonics Technologies, Chattanooga, TN, USA, 3–7 April 1995; International Space Planes and Hypersonic Systems and Technologies Conferences. American Institute of Aeronautics and Astronautics: Reston, VA, USA, 1995.
5. Traci, R.M.; Farr, J.L., Jr.; Laganelli, T.; Walker, J. *A Thermal Management Systems Model for the NASA GTX RBCC Concept*; NASA: Washington, DC, USA, 2002.
6. Lee, J.; Krivanek, T. Design and Fabrication of the ISTAR Direct-Connect Combuster Experiment at the Hypersonic Tunnel Facility. In Proceedings of the 43rd AIAA Aerospace Sciences Meeting and Exhibit, Reno, NV, USA, 10–13 January 2005; American Institute of Aeronautics and Astronautics: Reston, VA, USA, 2005.

7. Ju, S.; Yan, C.; Wang, X.; Qin, Y.; Ye, Z. Optimization Design of Energy Deposition on Single Expansion Ramp Nozzle. *Acta Astronaut.* **2017**, *140*, 351–361. [CrossRef]
8. Yu, K.; Xu, J.; Lv, Z.; Song, G. Inverse Design Methodology on a Single Expansion Ramp Nozzle for Scramjets. *Aerosp. Sci. Technol.* **2019**, *92*, 9–19. [CrossRef]
9. Hadjadj, A.; Onofri, M. Nozzle Flow Separation. *Shock Waves* **2009**, *19*, 163–169. [CrossRef]
10. Zebiri, B.; Piquet, A.; Hadjadj, A.; Verma, S.B. Shock-Induced Flow Separation in an Overexpanded Supersonic Planar Nozzle. *AIAA J.* **2020**, *58*, 2122–2131. [CrossRef]
11. Tomita, T.; Takahashi, M.; Sasaki, M.; Sakamoto, H.; Takahashi, M.; Tamura, H. Experimental Evaluation of Side-Loads in LE-7A Prototype Engine Nozzle. *Shock Waves* **2009**, *19*, 213–228. [CrossRef]
12. Nave, L.; Coffey, G. Sea Level Side Loads in High-Area-Ratio Rocket Engines. In Proceedings of the 9th Propulsion Conference; American Institute of Aeronautics and Astronautics, Las Vegas, NV, USA, 5–7 November 1973.
13. Frey, M.; Hagemann, G. Flow Separation and Side-Loads in Rocket Nozzles. In Proceedings of the 35th Joint Propulsion Conference and Exhibit, Los Angeles, CA, USA, 20–24 June 1999; American Institute of Aeronautics and Astronautics: Reston, VA, USA, 1999.
14. Verma, S.; Chidambaranathan, M.; Hadjadj, A. Analysis of Shock Unsteadiness in a Supersonic Over-Expanded Planar Nozzle. *Eur. J. Mech. B Fluids* **2018**, *68*, 55–65. [CrossRef]
15. Yu, Y.; Xu, J.; Yu, K.; Mo, J. Unsteady Transitions of Separation Patterns in Single Expansion Ramp Nozzle. *Shock Waves* **2015**, *25*, 623–633. [CrossRef]
16. Frey, M.; Hagemann, G. Restricted Shock Separation in Rocket Nozzles. *J. Propuls. Power* **2000**, *16*, 478–484. [CrossRef]
17. Watanabe, Y.; Sakazume, N.; Tsuboi, M. LE-7A Engine Nozzle Problems during Transient Operations. In Proceedings of the 38th AIAA/ASME/SAE/ASEE Joint Propulsion Conference & Exhibit, Indianapolis, IN, USA, 7–10 July 2002; American Institute of Aeronautics and Astronautics: Reston, VA, USA, 2002.
18. Östlund, J.; Damgaard, T.; Frey, M. Side-Load Phenomena in Highly Overexpanded Rocket Nozzles. *J. Propuls. Power* **2004**, *20*, 695–704. [CrossRef]
19. Baars, W.J.; Tinney, C.E.; Ruf, J.H.; Brown, A.M.; McDaniels, D.M. Wall Pressure Unsteadiness and Side Loads in Overexpanded Rocket Nozzles. *AIAA J.* **2012**, *50*, 61–73. [CrossRef]
20. Verma, S.B.; Haidn, O. Study of Restricted Shock Separation Phenomena in a Thrust Optimized Parabolic Nozzle. *J. Propuls. Power* **2009**, *25*, 1046–1057. [CrossRef]
21. Martelli, E.; Nasuti, F.; Onofri, M. Numerical Calculation of FSS/RSS Transition in Highly Overexpanded Rocket Nozzle Flows. *Shock Waves* **2010**, *20*, 139–146. [CrossRef]
22. He, M.; Qin, L.; Liu, Y. Numerical Investigation of Flow Separation Behavior in an Over-Expanded Annular Conical Aerospike Nozzle. *Chin. J. Aeronaut.* **2015**, *28*, 983–1002. [CrossRef]
23. Chutkey, K.; Viji, M.; Verma, S.B. Interaction of External Flow with Linear Cluster Plug Nozzle Jet. *Shock Waves* **2018**, *28*, 1207–1221. [CrossRef]
24. Li, J.; Chen, S.; Cai, F.; Yan, C. Numerical Investigation of Vented Plume into a Supersonic Flow in the Early Stage of Rocket Hot Separation. *Aerosp. Sci. Technol.* **2020**, *107*, 106249. [CrossRef]
25. Mousavi, S.M.; Pourabidi, R.; Goshtasbi-Rad, E. Numerical Investigation of over Expanded Flow Behavior in a Single Expansion Ramp Nozzle. *Acta Astronaut.* **2018**, *146*, 273–281. [CrossRef]
26. Lee, C.; Choi, K.; Kim, C.; Han, S. Computational Investigation of Flow Separation in a Thrust-Optimized Parabolic Nozzle during High-Altitude Testing. *Comput. Fluids* **2020**, *197*, 104363. [CrossRef]
27. Yu, Y. Over-Expanded Separation Transitions of Single Expansion Ramp Nozzle in the Accelerating and Decelerating Processes. *Aerosp. Sci. Technol.* **2020**, *98*, 105674. [CrossRef]
28. Yu, Y.; Mao, Y.; Yu, T.; Xu, S. Numerical Investigation on Mechanism of External Flow Field–Induced Separation Pattern Transition. *J. Aerosp. Eng.* **2023**, *36*, 04022123. [CrossRef]
29. Yu, Y.; Xu, J.; Mo, J.; Wang, M. Principal Parameters in Flow Separation Patterns of Over-Expanded Single Expansion RAMP Nozzle. *Eng. Appl. Comput. Fluid Mech.* **2014**, *8*, 274–288. [CrossRef]
30. Galván, S.; Reggio, M.; Guibault, F. Assessment Study of K-ε Turbulence Models and Near-Wall Modeling for Steady State Swirling Flow Analysis in Draft Tube Using Fluent. *Eng. Appl. Comput. Fluid Mech.* **2011**, *5*, 459–478. [CrossRef]
31. Smith, T.D.; Ill, F.C.; Rice, T.; Blaha, B. *Development of an Integrated Nozzle for a Symmetric, RBCC Launch Vehicle Configuration i35*; Glenn Research Center: Cleveland, OH, USA, 2000.
32. Campbell, B.T.; Siebenhaar, A.; Nguyen, T. Strutjet Engine Performance. *J. Propuls. Power* **2001**, *17*, 1227–1232. [CrossRef]
33. Tang, X.; He, G.; Qin, F. Investigation on Combustion Performance of Axisymmetric RBCC Combustor in Scramjet Mode. *J. Northwestern Polytech. Univ.* **2014**, *32*, 29–34.
34. Xue, R.; Hu, C.; Lv, X.; Qing, F. RBCC Constant Dynamic Pressure Booster Trajectory Design and Propellant Mass Flowrate Analysis for TSTO Transportation System. *J. Solid Rocket Technol.* **2013**, *36*, 155–160.